



OPEN

Influence of soil heterogeneity on soybean plant development and crop yield evaluated using time-series of UAV and ground-based geophysical imagery

Nicola Falco^{1✉}, Haruko M. Wainwright¹, Baptiste Dafflon¹, Craig Ulrich¹, Florian Soom¹, John E. Peterson¹, James Bentley Brown², Karl B. Schaettle³, Malcolm Williamson⁴, Jackson D. Cothren⁴, Richard G. Ham⁵, Jay A. McEntire⁶ & Susan S. Hubbard¹

Understanding the interactions among agricultural processes, soil, and plants is necessary for optimizing crop yield and productivity. This study focuses on developing effective monitoring and analysis methodologies that estimate key soil and plant properties. These methodologies include data acquisition and processing approaches that use unmanned aerial vehicles (UAVs) and surface geophysical techniques. In particular, we applied these approaches to a soybean farm in Arkansas to characterize the soil–plant coupled spatial and temporal heterogeneity, as well as to identify key environmental factors that influence plant growth and yield. UAV-based multitemporal acquisition of high-resolution RGB (red–green–blue) imagery and direct measurements were used to monitor plant height and photosynthetic activity. We present an algorithm that efficiently exploits the high-resolution UAV images to estimate plant spatial abundance and plant vigor throughout the growing season. Such plant characterization is extremely important for the identification of anomalous areas, providing easily interpretable information that can be used to guide near-real-time farming decisions. Additionally, high-resolution multitemporal surface geophysical measurements of apparent soil electrical conductivity were used to estimate the spatial heterogeneity of soil texture. By integrating the multiscale multitype soil and plant datasets, we identified the spatiotemporal co-variance between soil properties and plant development and yield. Our novel approach for early season monitoring of plant spatial abundance identified areas of low productivity controlled by soil clay content, while temporal analysis of geophysical data showed the impact of soil moisture and irrigation practice (controlled by topography) on plant dynamics. Our study demonstrates the effective coupling of UAV data products with geophysical data to extract critical information for farm management.

Precision agriculture has become an important strategy for improving crop micromanagement, maximizing productivity and optimizing resource allocation (i.e., smart use of irrigation, fertilizers, and pesticides)¹. Part of the innovation in precision agriculture is the use of sensing technologies such as remote sensing (satellite, UAV imaging), geophysics, and sensor networks. These technologies provide complementary information on environmental variables related to both plants and soil, through both direct and indirect measurements.

¹Climate and Ecosystem Sciences Division, Lawrence Berkeley National Laboratory, 1 Cyclotron Road, Berkeley, CA 94720-8126, USA. ²Environmental Genomics and Systems Biology, Lawrence Berkeley National Laboratory, 1 Cyclotron Road, Berkeley, CA 94720-8126, USA. ³Chemical and Biomolecular Engineering, University of California, 201 Gilman Hall, Berkeley, CA 94720-1462, USA. ⁴Department of Geosciences and Center for Advanced Spatial Technologies (CAST), University of Arkansas, Fayetteville, AR 72701, USA. ⁵Department of Industrial Engineering, 4207 Bell Engineering Center, University of Arkansas, Fayetteville, AR 72701, USA. ⁶Glennoe Farms LLC, Stuttgart, AR 72160, USA. ✉email: nicolafalco@lbl.gov

Remote sensing technologies have been extensively used in precision agriculture. In particular, the development of high-resolution satellite imagery systems (e.g., IKONOS (1999), QuickBird (2001), RapidEye (2008), WorldView (2007), and GeoEye (2008)) have provided resolutions ranging from about 2 to 5 m per pixel and improved revisiting time^{2,3}. Remote sensing data have been used to evaluate various agriculture practices, including (among others) water management in irrigated agriculture⁴, fertilizers and fungicide applications and their economic impact⁵, site-specific nitrogen fertilizer management⁶, and yield estimation for various crop types. However, the spatial resolution is still a limiting factor for studies that require information at plant/canopy scale. Weather conditions (in particular, cloud coverage) are also a critical impediment to satellite image acquisitions.

Recently, unmanned aerial vehicles (UAVs) have become readily available for agricultural applications^{7,8}. Compared to both satellite and airborne platforms, the UAVs' higher spatial-temporal resolution enhances our capability to study plant phenology in more detail, from leaf to crop scale⁹. Furthermore, the continuous introduction of UAV-specific sensors (e.g., multispectral and hyperspectral cameras, LiDAR sensors, thermal cameras) and their easy deployment provides the necessary planning flexibility to better characterize plant dynamics through the whole growing period and to avoid unfavorable weather conditions¹⁰. Among the different applications, UAV systems have been successfully used to monitor photosynthetic activities¹¹, assess water stress and nutrient deficits^{8,12}, estimate crop biomass¹³, canopy structures¹⁴, as well as identify crop diseases¹⁵. The ability to estimate plant-specific properties at the microscale (centimeter scale), such as plant counting and density^{16–19}, would also promote the identification of potential heterogeneous spatiotemporal patterns within crop fields. Such information can be beneficial in detecting areas that have unusual responses (e.g., low plant density, low plant development) to local agricultural practices.

In parallel, geophysics has been used for agricultural applications to derive near-surface soil properties²⁰. Geophysical methods, such as electrical resistivity tomography (ERT) and electromagnetic induction (EMI), have been widely used to extract near-surface and subsurface information as an alternative to expensive and time-consuming grid soil sampling^{21,22}. Soil properties—such as soil texture and composition, organic carbon content, and soil moisture—influence nutrient availability and biogeochemical activity, which in turn affect plant development and productivity. The soil apparent electrical conductivity (EC_a) measured by these systems is particularly sensitive to soil moisture, texture, and salinity, and therefore it can be used to estimate the spatial variability of the soil properties in heterogeneous environments^{20,23}. For example, soil EC_a has been used to map soil salinity and investigate the negative impact of high-salinity soil conditions on the crop yield²⁴. Soil EC_a has been used as a proxy both to estimate inorganic nitrogen²⁵ and to build a spatial model for organic carbon distribution²⁶. Soil characterization based on soil EC_a has been also used to delineate soil homogeneous zones for management purposes²⁷. Plant traits, such as ground-estimated leaf area index (LAI) and plant height were shown to correlate with soil texture spatial variability²⁸. It was also observed that such relationships vary, depending on the presence of dry or wet (year) conditions.

The joint use of remote sensing and geophysical data has been previously explored in natural ecosystems^{21,22,29,30}. It has been observed, for example, that plant phenotyping has a close relationship with belowground properties, such as soil composition and microbiology.

Remote sensing vegetation indices (VIs), such as the normalized difference vegetation index (NDVI) and the green chromatic coordinates (GCC), are well-known and widely used tools to characterize and monitor the plant vigor, which refers to the health status of a plant in terms of greenness, photosynthetic activity, biomass, and are found to exhibit a strong correlation to soil EC_a ³¹.

The combined use of geophysical measurements, LiDAR data, and vegetation indices allowed researchers to model complex relations between spatial patterns, biogeochemical activity, and carbon fluxes and to identify and characterize ice-wedge polygonal regions in an Arctic tundra ecosystem^{22,29}. Strong correlations between spatial variability in soil EC_a and plant community spatial distribution estimated by high-resolution satellite images were observed in mountainous watershed ecosystems³⁰ as well. The coupling of above- and belowground soil properties in agriculture ecosystems has been applied to better understand soil-plant interactions. A co-variability analysis between soil EC_a and satellite-derived LAI showed a general positive correlation following similar spatial patterns³². Recently, depth-specific soil EC_a and sun-induced fluorescent activity were jointly used to investigate soil-plant interactions³³, showing that the impact of soil at different depths on plant dynamics can be captured by using multicoil data inversions. In both studies, results showed that the soil moisture in the deeper soil highly impacted plant performance. A recent study found that ground-surface electromagnetic data were useful for estimating the spatial distribution of Bordeaux vineyard soil classes, and that the soil classes were spatially correlated with grapevine vigor estimated using airborne-based normalized difference vegetation index (NDVI) data³⁴.

Although there have been recent advances in UAV platforms and sensors, their potential has not been fully exploited for investigating soil-plant co-variability. While a few studies have proposed techniques to count plants^{16,35}, low and medium resolution satellite-derived products are often used for plant phenology and physiology characterization (i.e., plant's physical, structural, developmental, and physiological properties). However, there are few studies investigating early-season plant phenology and plant growth, and their relationship to soil properties. Early-season plant spatial abundance and plant vigor, which can be effectively estimated by high-resolution UAV image, are critical for identifying anomalous areas and for providing easily interpretable information for better decision making (e.g., replanting, reanalysing the irrigation system, etc.). In early season, plant coverage is expected to be spatially homogeneous, especially when the seeds are planted at an even distance. However, many factors can impact plant development from the emergence stage until the final reproductive stage of maturity, such as extreme local environmental conditions of soil moisture and temperature. Furthermore, it remains a challenge to integrate multiple sources of information to infer the properties of interest in agriculture that affect plant development. For example, to the authors' knowledge, there are no studies identifying key controls on plant growth or investigating the influence of initial plant assessment on crop yield by integrating

geophysics and remote sensing techniques. In addition, the temporal variability of aboveground-belowground properties represents another important aspect for investigating soil–plant relationships. Such relationships can be affected by the changes in soil conditions due to drought periods or heavy rains, and can be captured through time-lapse soil geophysical characterization.

In this work, we investigate the soil–plant interaction within an agricultural ecosystem—including crop yield—by taking advantage of high-resolution UAV data and spatially extensive geophysical data. We assess the impact of soil heterogeneity on the spatial–temporal variability of plant development and crop yield. For this purpose, we propose a novel framework that includes multi-source data integration of UAV-derived imaging and geophysical data. Our framework consists of three steps: (1) developing algorithms for high-resolution UAV images for mapping plant structural (height) and physiological information; (2) characterizing the soil–plant coupled spatial and temporal heterogeneity; and (3) identifying key controls on plant development and crop yield by investigating the co-variability between soil properties and UAV-derived products.

The particular emphasis is on estimating early-season plant signatures and geophysics-based soil characterization over the field. The proposed procedure estimates the plant spatial abundance by identifying the pixels associated with the plants and computing the ratio within a unit area. The discrimination between plants and soil allows us to improve the estimation of plant vigor by minimizing the background effect of soil. In this work, we used the GCC computed from a high-resolution RGB camera to estimate plant physiological dynamics and measured *in situ* high-resolution multi-depth soil EC_a to account for the soil spatial heterogeneity. We then investigate the co-variability among high-resolution UAV-derived products and soil EC_a to assess the impact of soil spatial heterogeneity on plant development. Geo-referenced yield maps are used to investigate the relationship between plant development and actual crop yield. To the authors' knowledge, this is the first study to integrate UAV and geophysical technologies to characterize spatiotemporal variability in both soil and plants, and to quantify their relationships to crop yield.

Materials and methods

We demonstrate our approach using an agricultural field under active commercial cultivation of soybeans located in the Arkansas Delta. For this study, we acquired time-series datasets of UAV and geophysical data during the 2018 growing season. This provided the opportunity to investigate the relationship between plant growth and spatially heterogeneous soil physical properties, as well as to analyse the temporal dynamics of such a relationship. All the methodology and data collection comply with relevant institutional and national legislation.

Site description and crop management. The investigated study area (34° 24.458' N, 91° 40.462' W), located in Humphrey, Arkansas, is a crop field of about 20 hectares that is under active commercial cultivation of soybeans (Fig. 1).

The study area is part of the Lower Mississippi River Basin's (LMRB) alluvial plain³⁷. This region is characterized by a wide range of cropland, such as soybean, corn, rice, grass, and pasture, supported by a humid subtropical climate with hot, humid summers and mild, slightly drier winters.

The crop field is adjacent to the oxbow Glenwood Lake (shown in Fig. 1) and is characterized by an alternating of Hebert silt-loam and Rilla silt-loam, according to the description provided by the gSSURGO map³⁸. The Hebert profile consists of a very deep, poorly drained, moderately slowly permeable soil that formed in silty alluvium, while the Rilla profile consists of a very deep, well drained, moderately permeable soils that formed in reddish silty and loamy alluvium.

High-quality soybean seed requires three appropriate conditions for germination—soil moisture, temperature and oxygen. Provided that the soil is not saturated, oxygen concentration is not a limitation, but germination will not occur in flooded soil due to lack of oxygen. Research shows that soybeans are in general very susceptible to soil saturation and anoxic conditions, which would provoke damage to the root system and in some case the termination of the plant growth³⁹.

Planting started on April 21st in rows (raised beds) with a spacing of 0.9 m. Plants reached their first vegetative stage of emergence (VE) on the first days of May and developed their first node with fully developed unifoliate leaves around mid-May (V1). The stage of initial bloom, which represents the starting of the reproductive stage (R1–R8) after the last vegetative stage, started in mid-June, reaching the full maturity (R8) about the end of September. Subsequent to R8, the leaves dry then fall from the plant at the time of harvest, which was performed on October 24th.

A common channeled (furrowed) surface irrigation approach was used as an irrigation system, which consists of a plastic pipe (polytube) located along one side of the field to deliver water into the channels between the rows⁴⁰. At the site, the plastic pipe was located on the east side of the field with the rows and furrows running east to west following the main slope gradient (Fig. 1) from east to west, in order to facilitate the water flow. Smoothing of the field's ground surface was performed prior to the planting to ensure a good surface drainage. Irrigation started on June 12th, after the rain period, and performed every 14 days.

Temperature and precipitation were measured by a weather station that we installed in the southeast corner of the field (Fig. 1). Based on the data collected, the average daily temperature increased from 14.6 to 24.7 °C between planting and the first vegetative stage (April–May), reached 27 °C during the vegetative period through the initial reproductive period (June–July), and decreased from 27 to 24 °C during the final period of maturity (August–September). The 2018 growing season was characterized by sporadic heavy-rain events, especially during the vegetative period (from April to mid-June), with a total cumulative precipitation (period April–September) of about 650 mm (Supplementary Figure S1). As a result of rain events, the soil moisture in April ranged from 0.17 (m³/m³) to 0.3 (m³/m³) (Supplementary Figure S2).

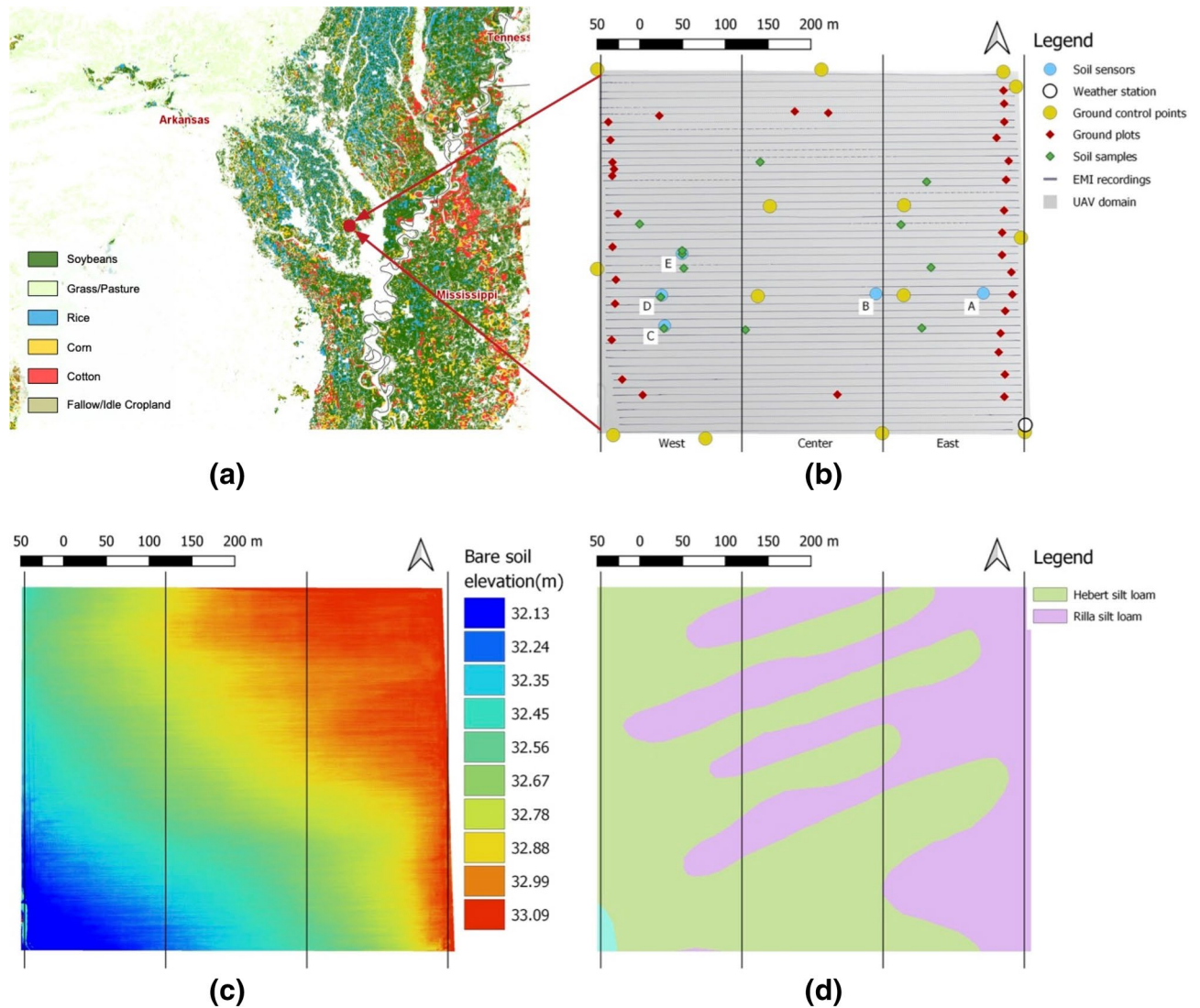


Figure 1. Study area located in Humphrey, Arkansas: **(a)** map produced by cropScape (USDA) showing part of the Delta region with the main agricultural land covers; **(b)** map of the field under study reporting the locations of the ground data collection; **(c)** map showing the topographic elevation derived by an UAV-based DEM, acquired acquisition prior to planting; **(d)** gSSurgo map provided by USDA, showing the soil types. Black vertical lines separate the east, center, and west sections used in the statistical analysis. Maps made with QGIS (v 3.6, <https://www.qgis.org>)³⁶.

Instrumentation, data acquisition, and preprocessing. *UAV-data acquisition.* Multitemporal image acquisitions were performed over the field using UAV-mounted sensors. The images were acquired on: May 8th, a few days after planting, May 28th, during the early vegetative development, and June 25th, July 23rd, September 19th, the beginning, middle, and end of the reproductive period.

We used the DJI Matrice 600 flying platform with the DJI FC350 on-board RGB (red, green, blue) camera as the primary image acquisition sensor. A flight plan to acquire high-resolution images at centimeter resolution was designed using this acquisition system. Flights were performed during the maximum Sun's elevation and with clear sky to avoid possible changes in light conditions, at an altitude of about 60 m, with a 75% image overlap, reaching a ground resolution of 2 cm.

In order to minimize the impact of possible variations in illumination conditions during each acquisition, two normalized mosaics were computed by using the pictures of a reference panel taken before and after each flight. The final mosaic was obtained by averaging the two normalized mosaics.

A total of 13 Ground Control Points (GCP) were positioned along the field perimeter and within the field for the mosaic reconstruction (Fig. 1). These consisted of flat targets and were surveyed at each acquisition with a Topcon real-time kinematic differential global positioning system (Hyper-V RTK-GPS). The system is composed of a rover and a fixed base station, ensuring high-resolution geolocation information at centimeter resolution. All the collected geolocation data were post-processed obtaining an average planar error of about 2 cm and a vertical error of about 3 cm.

We used the commercial PhotoScan (Agisoft) software for photogrammetry to construct the final mosaics. The software uses photogrammetry techniques based on structure from motion from multi-view stereo (SfM-MVS) images⁴². The processing produced mosaics with spatial resolution less than 10 cm, but the mosaics used in this work have a pixel size of 10 cm. Additionally, we used the software to compute digital elevation models (DEMs) from the RGB images with a final vertical resolution less than 5 cm.

Electromagnetic Induction (EMI) system. Soil EC_a was measured with an electromagnetic induction (EMI) system (CMD Mini-Explorer, GF Instruments), which consists of a transmitter and three receiver coils, allowing an effective acquisition of soil apparent electrical conductivity (EC_a) averaged across a depth range of 0.5 m, 1.0 m, and 1.8 m from the surface. The instrument provides soil EC_a measurements in milliSiemes per meter (mS/m) and the in-phase in parts per thousand (not considered in this study). The system was mounted in a sled pulled by an all-terrain vehicle and supported by a Differential Global Positioning System (DGPS) in order to tag each measurement with high-resolution positioning information. Time-lapse soil EC_a data collection was performed four times, including before and during the growing season: April 21st, May 12th, June 11th, and July 9th. EMI acquisitions were planned according to the irrigation plan and UAV acquisitions. Since the EMI instrument is sensitive to changes in soil moisture, we avoided the collection during or right after irrigation events. The data were acquired consistently every 10 rows with a distance between traverses of about 9 m.

In situ soil monitoring, ground imagery, and soil sampling. Soil sensors (5TE, METER) were used for continuous acquisition of volumetric water content (VWC) and soil temperature. The sensors were deployed in five areas (A, B ..., E, see Fig. 1) based on two factors: a) spatial variability of geophysical properties, b) differences in yield during the 2017 growing season (historical data available for this study). Each area has one logger that accommodates 4 sensors within a maximum radius of 4 m. To capture both shallower and deeper soil dynamics, we positioned 2 sensors vertically aligned at the depths of 12 cm and 25 cm on both the south (side1) and north (side2) of the logger. The areas A and D were positioned in high and low soil EC zones, respectively, while B was in an area of transition. Sensors A, B, and D were positioned along the same rows to form two transects, one on the south and one on the north. Sensor E was positioned within a very low 2017 yield in the west side of the field but at a mid-range of soil EC values. The logger C was positioned across a soil EC boundary, but it stopped recording data at early season and was discarded from this analysis. The collected temperature data are used to correct the EMI acquisitions, whereas soil moisture is used to track the irrigation events and possible saturations. As a support system for the sensors' data transmission, we used EM60G (METER) data loggers and ZENTRA cloud (METER) for cloud data storage.

Ground RGB images were taken at several plots (Fig. 1) for ground-based plant spatial abundance assessment. We used a wooden-frame of 1 m by 1 m to delimit the plot's area and took a picture from above (1.4 m from the ground). This assessment will be used to validate UAV-based plant spatial abundance estimates.

Soil samples were collected at twelve locations (Fig. 1). Physical laboratory testing was performed at the Fayetteville Agriculture Diagnostic Laboratory of the University of Arkansas to characterize soil properties, such as clay density, porosity, dry bulk density, volumetric water content, and organic matter. Such information was used for statistical analysis and to provide an interpretation of the soil EC_a measurements. No plant tissues or seeds were collected in this study.

Yield data from a combine harvester. Crop yield was harvested on October 24th. The combine harvester recorded yield information as cloud-point data in bushels per acre (bu/ac) and reported here in kilogram per hectare (kg/ha), and the relative geolocation information. The combine harvester is able to collect 11 rows at once and records a point measurement every 2 s. Areas with artefacts were determined based on the swath parameter recorded during the harvesting. The wrong choice of the swath parameter on the combine harvester would produce unreliable yield values. Such areas were not considered in further analysis.

Methodology. We designed a data analysis framework to combine the UAV optical images and soil geophysical measurements for characterizing plant phenological and physiological properties and soil spatial heterogeneity, respectively. We then performed statistical analysis of their co-variability to quantify the influence of soil properties on plant development. This framework is constructed by the following three steps:

1. UAV-based monitoring of plant dynamics: This step presents the data processing pipeline used for computing UAV products to characterize plant phenology and structure, such as plant spatial abundance, plant-specific vigor, and plant height.
2. EMI-based monitoring of soil characterization: This step focuses on quantifying the soil spatial variability. We perform statistical analyses to identify the relationship between soil EC_a signal and textural information derived by soil samples collected during the ground data acquisition.
3. Quantifying soil-plant spatiotemporal co-variability: This step focuses on the statistical analysis of plant physiological and structural properties and near-surface properties, as well as identifying key environmental factors.

UAV-based plant monitoring. Figure 2 depicts the data processing pipeline developed to assess the spatial variability of plant characteristics during the growing season. The steps to obtain the plant spatial abundance and plant vigor maps are presented in detail in the following sections.

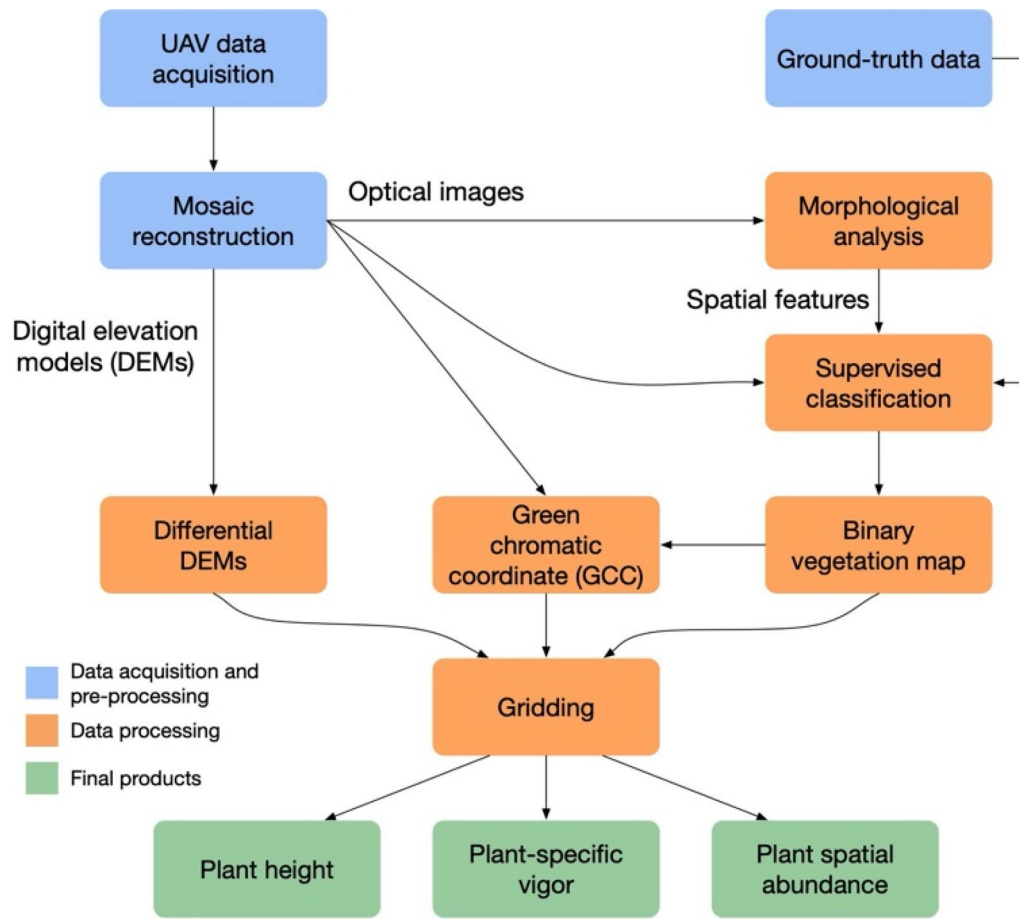


Figure 2. Pipeline developed for the UAV data processing.

Plant spatial abundance. Plant spatial abundance is estimated by the RGB mosaics. In the first step of the procedure, a vegetation map was obtained by performing a binary classification to discriminate the two classes of vegetation and soil. We used a supervised spectral-spatial image classification approach⁴³ that combines both the spectral and the contextual (i.e., geometrical) information. The contextual information represents the pixel spatial arrangement and the spatial relationship between adjacent pixels. By modelling such information, we can extract structures within the scene. For this step, we use mathematical operators, such as attribute profiles^{44–46} that belong to the image processing sub-field of mathematical morphology. Such operators are 2D filters that act on regions of connected pixels based on the evaluation of an attribute (e.g., scale, defined as number of pixel composing the region). The advantage of using this operator is the ability to preserve the geometrical detail of the structures in the scene. In a filtered image (or feature), regions with similar properties (i.e., scale) are preserved or otherwise merged to their surroundings (i.e., filtered). A multiscale contextual characterization is obtained by applying a filter recursively and relaxing the scale parameter of the filter at each iteration, resulting in a stack of filtered images. An automatic procedure developed in⁴⁵ is used to perform such a characterization. Such operation serves to extract homogeneous structures present in the scene at different spatial scales, allowing us to better delineate the soybean rows. The original RGB image, together with the filtered images, compose the feature space used as input to a support vector machine (SVM) algorithm with a radial basis function (RBF) kernel. The algorithm is based on the LIBSVM library⁴⁷ developed for the MATLAB environment, using a one-against-one multiclass strategy. In a second step, we compute the spatial abundance of the detected plants as the percentage of pixels that belong to the vegetation class within a grid unit. In our study we chose a grid unit of 2 by 2 m, which would allow to obtain a good approximation of the local change, while capturing large scale patterns. The quality of the plant spatial abundance map is mainly dependent on the performance of the classification algorithm used to separate the plants from the soil in the background. To validate this product, we computed the classification performance based on ground-truth data and compared the UAV-based estimates of plant abundance to ground-based assessments. The ground assessment of the plant spatial abundance was performed by selecting 31 plots in conjunction of the UAV acquisition occurring in May 28th, 2018. The plots were located mainly along the east and west sides of the field within a distance that ranges between 12 and 25 m from the edge of the field towards the field center; and some plots were collected along the south and north sides within a distance of 50 m from the field edge. These plots were selected to capture representative spatial abundances, ranging from 0% (almost bare) to 60%. Ground images were systematically taken at a height of 1.4 m from the ground. From these images, we computed the GCC and identified a threshold to separate the plant covered area from the soil back-

groun. The plant spatial abundance was then computed as the percentage of pixels identified as soybean over the entire area of the plot. All the ground-data were geolocated using the RTK-GPS system previously described.

Plant-specific vigor estimation. Remote-sensing-derived VIs have been extensively used as a proxy to estimate plant vigor and investigate plant physiology and response to possible ecosystem changes. Widely used VIs for plant characterization are in general derived by the near-infrared (NIR) channel (e.g., NDVI, SAVI, etc.), which is sensitive to changes in chlorophyll and leaf area. However, RGB-based indices have been developed and used in several phenology studies, showing their effectiveness in estimating plant characteristics compared to NIR-based VIs⁴⁸. The GCC was chosen based on authors' recent studies, showing that this RGB-based VI is less affected by saturation compared to NDVI³¹. GCC is formally defined as follows:

$$GCC = \frac{G_{DN}}{B_{DN} + G_{DN} + R_{DN}}, \quad (1)$$

where R, G, and B are the red, green, and blue channels, and DN refers to the pixel intensity values as digital numbers⁴¹. The plant-specific vigor was computed considering only those pixels identified as vegetation, the information for which is provided by the binary classification. In order to have products spatially comparable, the plant-specific vigor was transformed into a 2 by 2 m grid by computing the average within each grid unit. This procedure has the advantage to minimize the soil component in estimating plant vigor, avoiding the non-uniqueness of lower productivity versus increased soil coverage. Specifically, it allows a more accurate way of capturing the spatial variability of the plant's vigor, in particular during the early vegetative stage, when the soil component is overabundant compared to the plant spatial abundance. This is a clear advantage over a satellite-derived VI with a coarser resolution that would provide an underestimation of plant vigor due to soil coverage.

Plant height estimation. Plant height was computed by subtracting the digital elevation model (DEM) of bare soil (i.e., reference DEM) from the digital surface model computed at each acquisition. The reference DEM was computed from acquisition occurred on May 8th, which was planned a week after planting so that it is not affected by surface disturbances by the planter. DEMs were computed using the PhotoScan software (Agisoft) during the mosaic reconstruction phase. We assume that the ground surface elevation stays the same during the growing season.

EMI-based soil characterization. We used the EC_a data to evaluate the spatial heterogeneity of soil properties and the temporal variability in soil moisture. We primarily used the EMI measurements associated with the 1 m effective depth, which is the depth range expected to encompass the soybean roots. Temperature corrections were applied to the point-cloud data for correcting the measured soil EC_a to the reference temperature of 25 °C. We employed the exponential model presented in Corwin and Lesch⁴⁹ and developed by Sheets and Hendrickx⁵⁰, and formally described as follows:

$$EC_{25} = EC_a \cdot \left[0.4470 + 1.4034e^{(-T/26.815)} \right], \quad (2)$$

where EC_{25} represents the corrected soil EC_a at the reference temperature of 25 °C, EC_a represents the measured soil EC_a, and T represents the soil temperature at the time of the acquisition. The model was chosen based on the on the methodological comparison⁵¹, which shows that the exponential model provides very similar estimations compared to the widely used ratio model^{31,52} in the temperature range of 3–43 °C, but with a smaller total residual.

A spatial correction was applied to the data to resolve a spatial shift caused by the distance from the EMI instrument and the actual position of the GPS antenna, which were 4.5 m apart due to the system setup. We performed statistical analysis between EMI data and soil samples collected during the April data acquisition to identify the main control on the spatial variability of soil EC_a.

Co-variability among plant and soil signatures. We performed a suite of statistical analyses, based on the high-resolution data layers, on soil and plant characteristics (i.e., plant spatial abundance, plant vigor, plant height, soil EC_a, and crop yield) to investigate the impact of soil properties on plant development during the growing season. For the analysis, we considered the yield point-cloud data as geo-reference.

Since the EMI and crop-yield data had a lower vertical resolution (along the y axis) of about 10 m (distance between rows selected for the data collection), we computed the average of each metric within a window of 20 m by 20 m. The exploratory data analysis included run charts and scatter plots to investigate the temporal evolution of plant development during the growing season, and the co-variability between plant characteristics and soil EC_a. We evaluated the correlation between variables using Pearson's correlation, as well as their spatial association. To control for the spatial non-independence, we derived a corrected Pearson's correlation by using the hypothesis testing procedure proposed by Clifford, Richardson, and Hémon (1989)⁵³. The method uses Moran's I⁵⁴ to compute the spatial autocorrelation in the spatial data sets and estimate the correct degrees of freedom, which are then used to assess the significance of the correlation. The method uses the Sturges' formula to identify the number of distance classes⁵⁵.



Figure 3. Time-lapse of UAV-RGB image acquired during the growing season (May 28th, June 25th, and July 23rd), and the point-cloud maps of the yield (kg/ha) acquired by the combine harvester (right figure). Maps made with QGIS (v 3.6, <https://www.qgis.org>)³⁶.

Results

UVA-derived products: plant spatial abundance, plant-specific vigor, and plant height. Figure 3 shows the reconstructed multitemporal RGB mosaics at a spatial resolution of 10 cm, acquired over the field in May 28th, June 25th, and July 23rd, and the point-cloud yield map acquired by the combine harvester.

From each acquisition, DEMs were also extracted at the same pixel resolution. Plant spatial abundance, plant-specific vigor, and plant height (Fig. 4) were estimated from the RGB dataset shown in Fig. 3. All the computed products show a spatial heterogeneity in plant development over the growing season. Although plant spatial abundance and vigor generally increase over the growing season, the images clearly show persistent areas where plant spatial abundance and vigor remain low (depicted in dark colours, e.g., northwest, southeast). The products also identify areas where plant-specific vigor and plant spatial abundance degraded in the late part of the season; particularly in the west-center area of the field. Similarly, the plant height maps, which were computed for the acquisitions of June 25th, July 23rd, and September 19th, show how plant structure and development follow specific spatial patterns.

The performance of the binary classification used to compute the plant spatial abundance and plant-specific vigor is assessed in terms of class accuracies, overall accuracy, and kappa coefficient averaged over fivefold. The metrics are reported in Table 1, together with the relative standard deviations. A quantitative assessment of the plant spatial abundance estimation was performed by investigating the correlation between the plant spatial abundance estimated via UAV and the one estimated based on ground observations. The validation analysis based on the 31 plots, depicted in Fig. 5, provided a R^2 of 0.82, indicating that the UAV-based estimations of plant spatial abundance can explain most of the ground measurements' variance. The significance of this result is supported by a p-value of 2.66×10^{-12} . The figure also indicates the residual for each sample, whose standard deviation (root mean square error—RMSE) is about 7.89. A few examples of the ground estimation and relative UAV-based estimations are depicted in Fig. 6, which reports the estimations for both ground and UAV-based estimations.

Geophysical data analysis. Figure 7a shows the interpolated soil EC_a data after applying the temperature and spatial corrections for top 1 m of soil. The maps reveal the alternating high and low soil EC_a regions in a diagonal pattern, represented by blue and red colours, respectively. This pattern is in agreement with the one shown in the gSSurgo map as well as the soil type division (shown on the April acquisition), with Hebert profile coinciding with high soil EC_a areas. The overlap between SSurgo map and our geophysical survey shows a great agreement but also a mismatch between the soil type boundaries. The soil EC_a ratio maps (Fig. 7b) computed between consecutive acquisitions provide a visual interpretation of the possible temporal-spatial variability of soil properties. From the maps, we can see that soil EC_a is consistent from April through June (Fig. 7b, left and center), with the ratio maps showing a slightly general decrease in soil EC_a . A large shift in soil EC_a is visible in the west area in the June–July ratio map (Fig. 7b, right). The increase in the ratio (shown in red colour) indicates a decrease in the soil EC_a measured in July, due to a possible decrease of soil moisture. Such a decrease is confirmed by the in situ soil-moisture sensors in the east and west regions (Supplementary Figure S2), showing that the irrigation events are well recorded by sensors located at the east side (A1 and A2), whereas the irrigation at the west side (D1 and D2) seems less effective for both shallower and deeper sensors.

To better understand the soil EC_a data, we performed a statistical analysis between the soil EC_a collected in April and the soil properties derived by the analysis of the soil samples, such as clay density (g/cm^3), porosity (%), dry bulk density (g/cm^3), volumetric water content (VWC) (%), and organic matter density (g/cm^3). The resulting correlation matrix (Fig. 8) shows that soil EC_a correlates mainly with clay density, which can be seen as an indicator of water retention and of soil with poor drainage properties, as clay density correlates with VWC.

Co-variability between plant characteristics, soil EC_a , and yield. The results from the analysis of UAV-products showed heterogeneous spatial patterns in terms of plant development. This can be seen in the time series collected during the growing season, shown in Fig. 6, in which plant spatial abundance, plant-specific vigor, and plant height vary drastically within the crop. Such heterogeneity is investigated in more detail in Fig. 9,

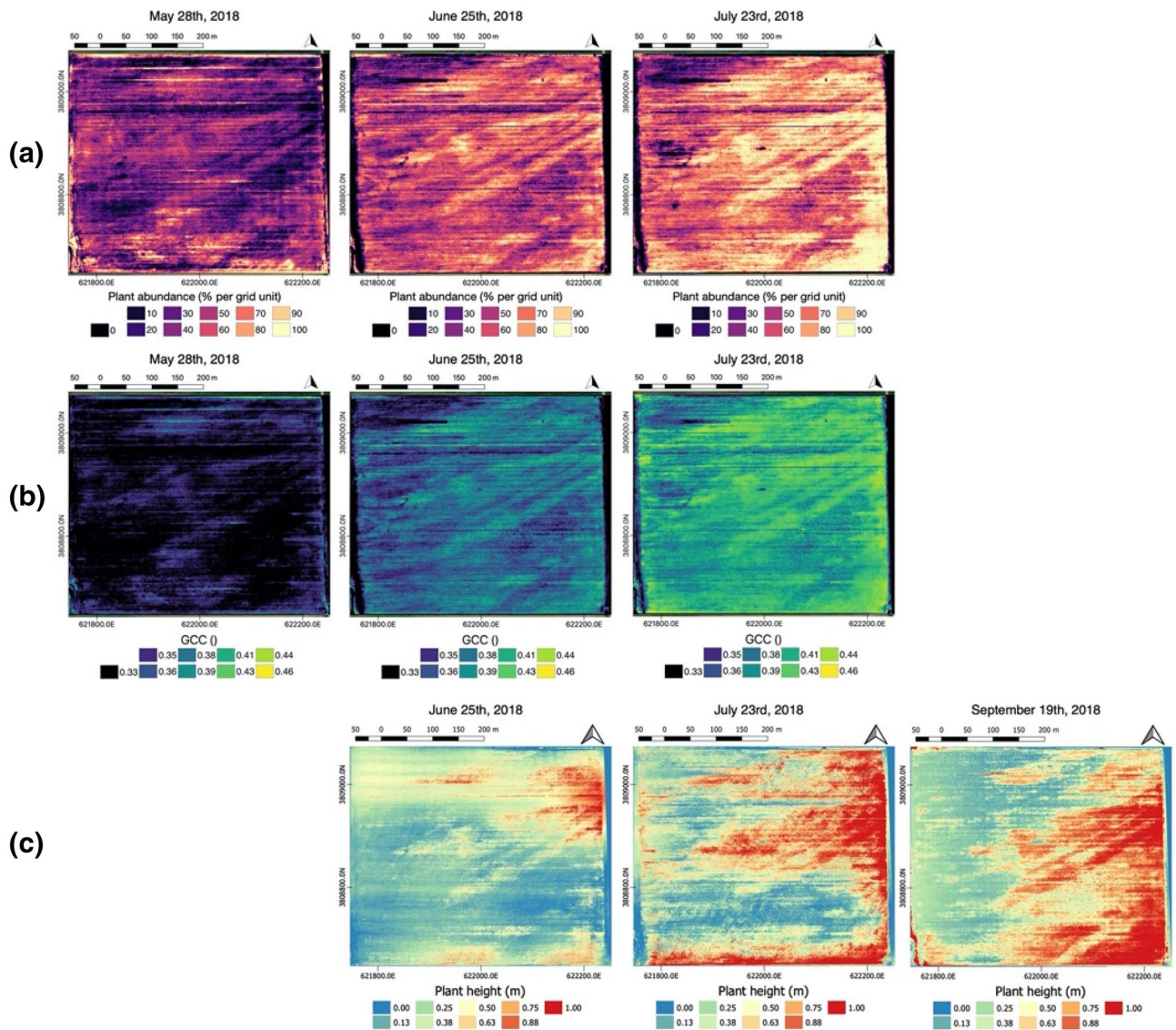


Figure 4. UAV products consisting of: (a) plant spatial abundance; (b) plant-specific vigor represented by the GCC index; and (c) plant height. The maps are vertically aligned according to their temporal acquisition. Maps made with QGIS (v 3.6, <https://www.qgis.org>)³⁶.

Class	Training set	Test set	Accuracies
Plant	1000	2400	99.26% (0.01)
Soil	1000	2400	99.23% (0.02)
OA (%)			99.25% (0.01)
k			0.98 (0.01)

Table 1. Performance of the binary classification to estimate the plant and soil coverage.

which reports the analysis of the time-series collected during the growing season. To capture the topographic gradient, the field was divided into three sections, east (higher in elevation and close to the water pump), center, and west (lowest in elevation and far from the water pump) (Fig. 1). Such a division has been commonly used in hillslope hydrology and biogeochemistry studies, which focuses on water flow, soil moisture, and associated biogeochemical processes^{57, 58}. Alternative methodologies, such as clustering, can be used to identify regions that show specific temporal-spatial soil-plant dynamics⁵⁹. Within each section, we capture the heterogeneity in soil texture by identifying areas of high and low soil EC_a according to the acquired geophysical data and quantified the impact on plant development by comparing plant properties within these areas. Here, we used the soil EC_a data

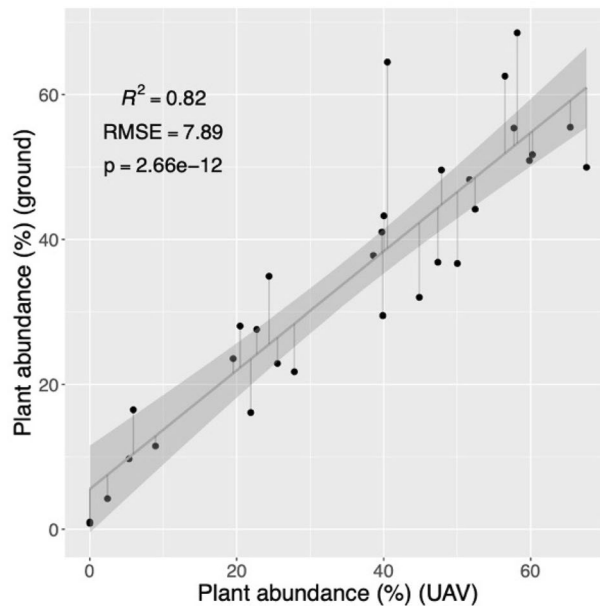


Figure 5. Scatterplot between ground and UAV-based plant spatial abundance. The analysis shows a high R^2 , indicating a strong agreement between the two estimations, which is also supported by a significant p-value. The scatterplot also shows the residuals, whose standard deviation is about 7.89 (RMSE).

acquired in April, as it is not affected by management activities, such as irrigation, and the signal would be driven mainly by soil texture.

The results of the analysis indicated a general decline of plant vigor, spatial abundance, and height from east to west. While plant vigor and spatial abundance consistently increase for the east and central areas from May to July, these plant properties only slightly increase for some of the locations in the west section, and even decline for others in the west. Such a decline can be seen as early as June. Each section is characterized by a different temporal behaviour, with plant spatial abundance and vigor strongly correlated. The highest values of plant spatial abundance, plant-specific vigor, and plant height are observed in low EC_a areas within the east section, whereas the west section corresponds to the lowest growth rate. In west section, where the plant performance are much lower compared to both the east and center areas of the field, the relationship soil EC_a /plant performance is inverted, with higher plant spatial abundance and vigor coinciding with high soil EC_a .

We investigated the relationship between the temporal variability of soil EC_a computed as ratio (Fig. 7b), and yield (Fig. 3). The soil EC_a ratio is used here to account for a possible decrease in soil moisture. The result of this comparison, depicted in Fig. 10, shows a quite different density distribution in yield (lower values) in the west area compared to the east and center areas. The negative correlation between crop yield and the ratio of soil EC_a of June and July indicates the decrease of soil moisture is linked to the decrease in the yield compared to the east and center areas. Such conditions produced a yield of one-third less than the one of the previous growing season (Supplementary Figure S3).

We further investigated the correlations between soil EC_a and the various plant properties by evaluating the Pearson's correlations (r) and the corrected Pearson's correlation (corr) based on Clifford's methods. The results of the analysis (Table 2) indicate a general negative correlation between soil EC_a and the plant spatial abundance, the plant vigor, and the plant height such that lower soil EC_a is associated with higher plant spatial abundance, vigor and height. During the growing season, the negative correlation becomes more pronounced during the summer period, particularly in the east and center sections. There are differences among east, center, and west sections. The negative correlation is smaller in the west section. The negative correlation is consistent in the center and east sections. In the western section, the magnitude of the correlation drops between June and July, implying a major shift has occurred. The results from the Clifford's method, which consider the spatial association between spatial datasets, showed that plant height is not significantly correlated with soil EC in the east areas. We also investigated the correlation between elevation and soil EC. The results of the analysis showed a non-significant correlation between elevation and soil EC, when spatial association between the two datasets is taken into consideration.

The results of the analysis of the relationship between yield, plant properties, soil EC_a , and elevation are reported in Table 3. The results show a general positive correlation between yield, plant spatial abundance, vigor, and height such that the higher plant spatial abundance, vigor and height are associated with higher yield, in particular during the summer period. The corrected correlation confirmed the significance in most of these cases. Elevation resulted not significantly correlated to yield, when spatial association is considered.

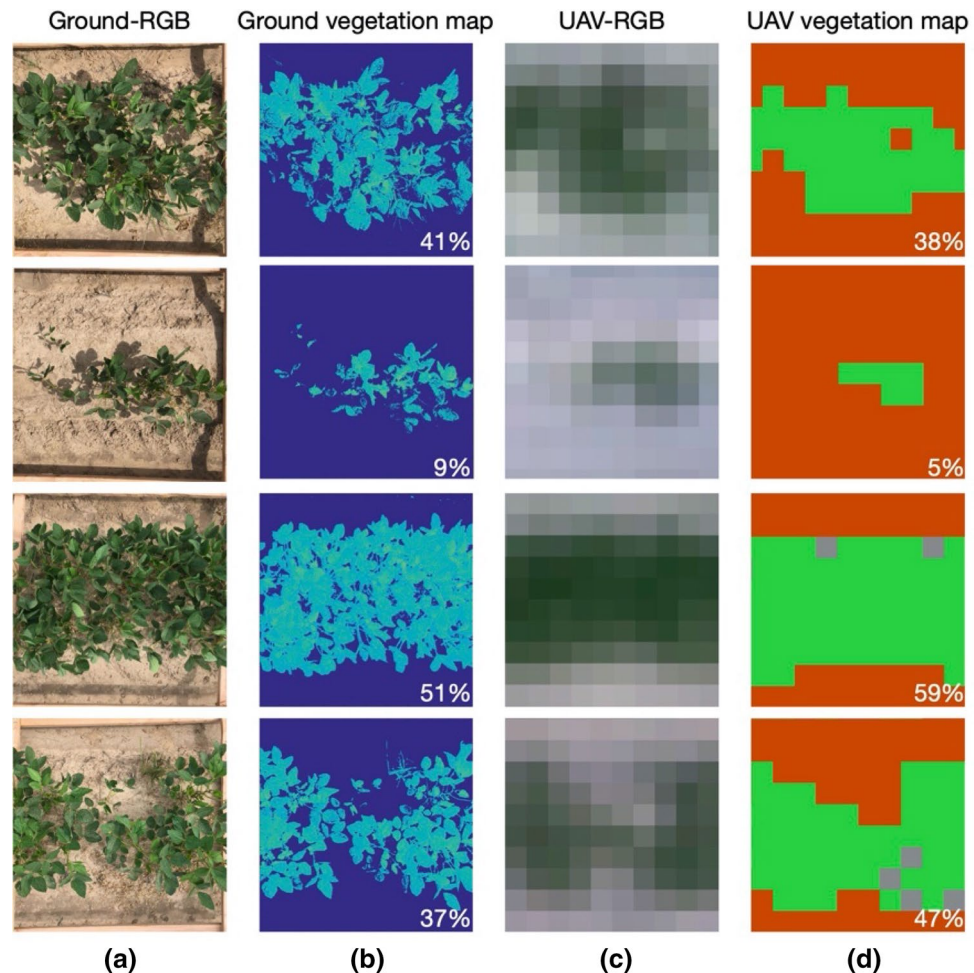


Figure 6. Ground assessment of the performance of the algorithm for extracting vegetation and computing the plant spatial abundance: (a) ground images of the plots captured by an RGB camera; (b) extraction of vegetated area for plant spatial abundance estimation; (c) UAV-RGB portion that covers the plot; (d) vegetation map obtained by the proposed method to estimate the plant spatial abundance, where green, red, and grey represent the vegetation, soil, and the unclassified classes, respectively. The estimated plant spatial abundance are reported for each case. Maps made with MATLAB R2017a (1994–2020 The MathWorks, Inc.)⁵⁶.

Discussion

This study explored the integration of remote sensing and geophysics to investigate the above/below-ground or soil–plant dynamics that influence plant growth and harvest yield in an agricultural ecosystem. To capture the plant dynamics, we proposed a novel UAV data processing pipeline to estimate plant spatial abundance and plant-specific vigor using high-resolution images (10 cm per pixel). We captured the soil texture and soil moisture variability using surface EMI surveys. Although both technologies—UAV and EM—have been used extensively in agriculture, the major contribution of this study is the integration of these datasets to enhance our understanding of the spatiotemporal variability of soil–plant interactions and to identify the main drivers on crop yield.

In this work, we use an RGB camera to extract plant characteristics, such as plant spatial abundance, plant height, and plant-specific vigor, as well as topographic properties. Plant spatial abundance was computed as the area occupied by the plants within a grid unit, where plants were detected by using a machine-learning based classification approach that exploits spectral and spatial features information. By applying this method to sub-meter resolution UAV images, we were able to estimate plant spatial abundance since the early stage. Such information is critical to identify anomalous areas, where the plant development is affected. Because in early stage, plants are spatially separated, the resulting abundance map can be used to provide an estimate of the sprout density. The plant-specific vigor was computed considering only pixels associated with plants extracted during the plant spatial abundance estimation. This allowed us to minimize the effect of the soil when averaging into the grid unit and preserve plant-specific greenness information.

Although the plant spatial abundance and plant-specific vigor are expected to provide independent information, they are highly correlated. One reason is that high plant spatial abundance areas are expected to have plants with higher biomass, and bigger leaves, which also influences the spectral signal and the computation of the

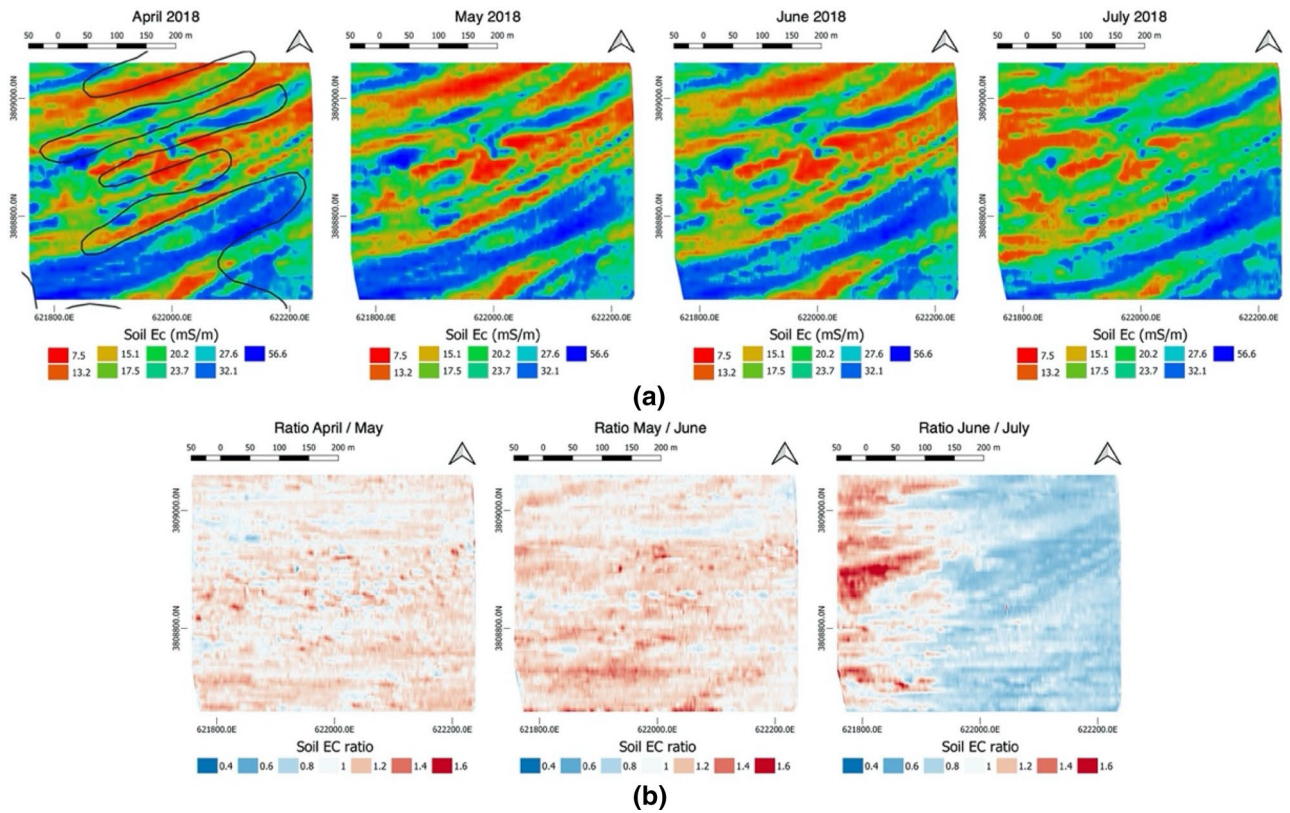


Figure 7. (a) Time-series of soil EC_a acquired during the growing season. (b) Maps of the soil EC_a ratio between adjacent data collection. The soil EC_a seems consistent between April and June, showing an almost uniform slight decrease (ratio about 1.2). A strong variation can be noticed between June and July, with the west area becoming dryer. The black lines overlapped on the april acquisition represent the gSSurgo boundaries. Maps made with QGIS (v 3.6, <https://www.qgis.org>)³⁶.

GCC. Additionally, low plant spatial abundance areas are characterized by plants with few or smaller leaves and possibly with more woody parts exposed, which again would decrease the values of plant vigor in these areas.

Plant height was the third metric for plant characterization computed from the RGB images, based on structure-from-motion methods and it is a measure of the plant structure. To minimize the estimation error, we use an RTK-GPS system to ensure that UAV acquisitions are co-registered with errors in x, y, and z around the centimeter scale. Plant height had a similar behaviour to plant spatial abundance and plant-specific vigor, although the difference between low/high soil EC_a areas in the east and center sections is more pronounced. This would indicate that plant height, which is a proxy for plant structural information, is more sensitive to water stress due to changes in the environment, such as soil moisture content, affecting the physiology of the plant.

The geophysical surveys based on EMI system provided a high-resolution image of the spatially heterogeneous soil properties of the field under study. The temperature and spatial shift corrections were necessary to provide a reliable interpretation of the readings. In particular, the temperature correction is critical when investigating the spatial-temporal variability of soil EC_a due to variability in soil moisture⁵². Our EMI data was effectively used in our analysis to capture the soil moisture shift in the west section, which caused the changes in the correlations between soil and plant signatures.

The analysis showed that the spatial heterogeneity in plant spatial abundance, plant-specific vigor, and plant height was influenced by soil textural variability (clay content; represented by high/low EC_a), soil moisture, and topographical gradient (represented by west, center, east sections). In particular, soil EC_a was negatively correlated with plant spatial abundance, and plant-specific vigor, indicating that areas with higher clay content (higher EC_a) have a negative impact on the plant development. Plant height resulted negatively correlated, however resulted not significant within the east and west sections, when spatial association is considered. The general negative correlation between plant properties and soil EC could be attributed to short-term soil water saturation during the irrigation period caused by the irrigation system based on furrow. The saturated soil in clay-rich regions with a slow drainage could particularly limit the soil oxygen uptake, negatively impacting the plant development³⁹. Such conditions may not apply to other crops with a deeper root system³³. It is worth noting that while topographic gradient represents the main driver on water distribution, it is not aligned with either soil EC_a measurements and gSSurgo soil map (as shown in Fig. 7a and supported by the statistical analysis in Table 2).

The correlation between soil EC_a and plant signatures is consistent over time but heterogeneous; the correlation in the west section decreased in July. Such a shift was due to a change in soil conditions that affected plant development. The change was captured by both the UAV-based products and the geophysical survey. The plant

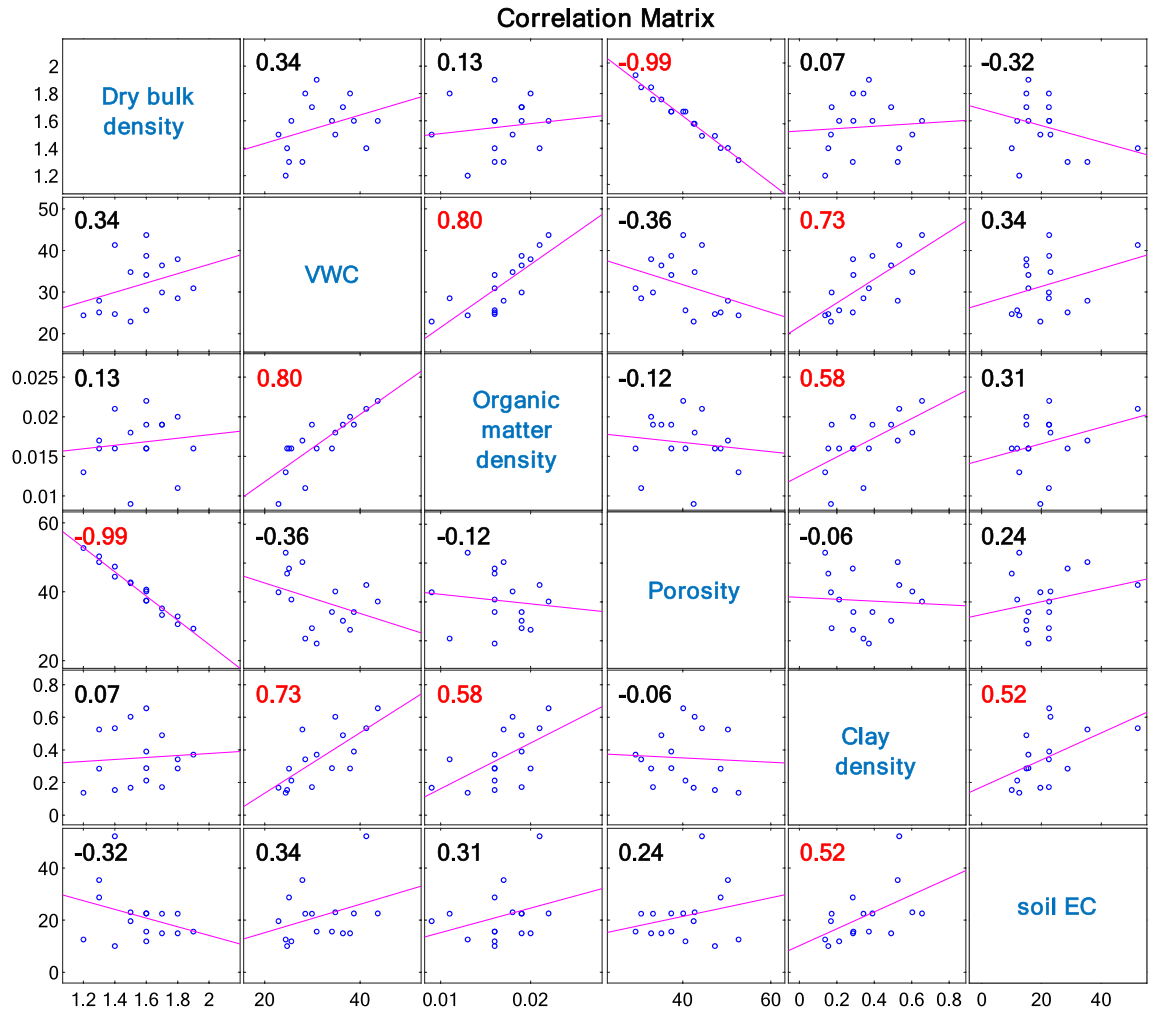


Figure 8. Correlation matrix between soil EC_a and soil properties: dry bulk density (g/cm³), volumetric water content (VWC) (%), organic matter density (g/cm³), porosity (%), and clay density (g/cm³). Values that are significant are shown in red (alpha=0.05).

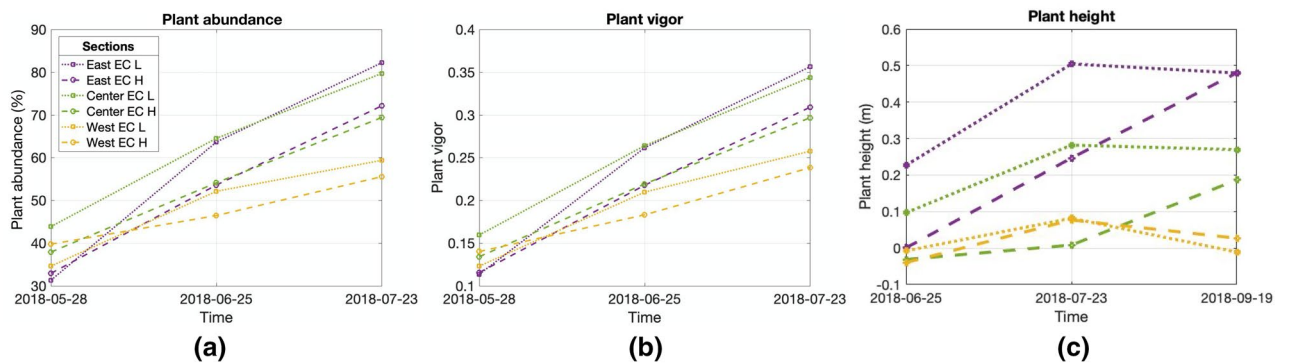


Figure 9. Run charts for time series of plant characteristics: (a) plant spatial abundance; (b) plant-specific vigor computed in terms of GCC index; (c) plant height. The data are reported as average values for each of the three sections (east, center, west, identified by different colors), considering high and low values of soil EC_a.

spatial abundance and plant height showed a decrease in performance in the west area during the early maturity period, indicating the interruption of the plant growth. Using the time-series EMI data and applying the ratio between acquisitions, we were able to capture the decrease of soil moisture and its spatial extent, which in turn affected the plant development in that area. The change in soil conditions occurred after June can be attributed

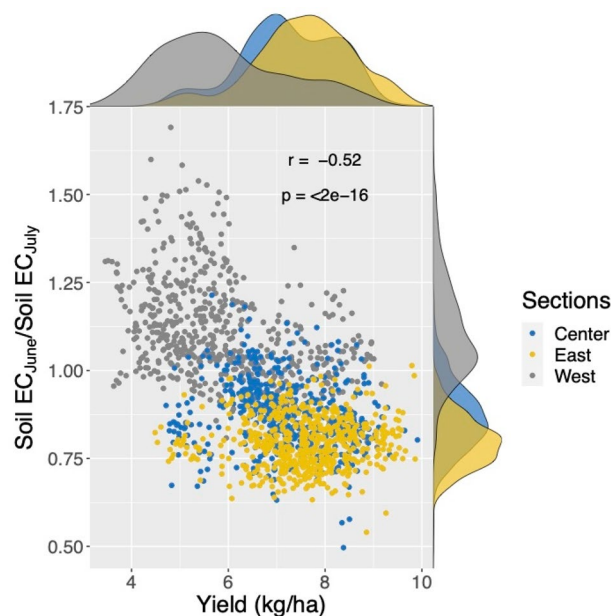


Figure 10. The negative correlation between crop yield (kg/ha) and the ratio of soil EC_a of June and July shows the decrease in crop yield corresponding to the decrease in soil moisture in the west area.

	Date	West		Center		East	
		r	corr	r	corr	r	corr
Soil EC versus plant spatial abundance	2018-05-28	0.23***	-0.09 (-)	-0.36***	-0.41***	-0.03 (-)	-0.03 (-)
	2018-06-25	-0.22***	-0.35***	-0.56***	-0.66***	-0.52***	-0.57***
	2018-07-23	-0.01 (-)	-0.1 (-)	-0.51***	-0.57***	-0.49***	-0.48**
Soil EC versus plant vigor	2018-05-28	0.21***	0.07***	-0.40***	-0.45***	-0.02 (-)	-0.08 (-)
	2018-06-25	-0.24***	-0.37***	-0.57***	-0.66***	-0.53***	-0.58***
	2018-07-23	-0.03***	-0.13***	-0.54***	-0.59***	-0.50***	-0.50**
Soil EC versus plant height	2018-06-25	-0.20***	-0.22 (-)	-0.51***	-0.56***	-0.58***	-0.60 (-)
	2018-07-23	-0.09*	-0.11 (-)	-0.52***	-0.49***	-0.53*	-0.49 (-)
	2018-09-19	-0.34*	-0.05 (-)	-0.29***	-0.34 (-)	-0.11*	-0.10 (-)
Soil EC versus elevation		-0.49***	-0.38 (-)	-0.32***	-0.32 (-)	-0.57 (-)	-0.60 (-)

Table 2. Pearson's (r) and corrected Pearson's (corr) correlation coefficients computed between the average soil EC_a, plant properties, and elevation. The table reports the correlations computed for the east, center, and west areas. Statistical significance is given by * $p < .05$, ** $p < .01$, *** $p < .001$, (-) for non-significance.

to the cumulative results of the few precipitation events during the vegetative stage and to the non-uniform irrigation, for which topographical gradient represented the main control.

Part of our analysis was to understand the link between soil–plant dynamics and crop yield. The negative correlations between yield and soil EC_a in the east and center areas showed the impact that soil texture has, not only on the plant development, but also on the final yield. Because of the water limiting scenario in the west area, results reported a positive correlation between areas with higher clay content and crop yield, as these areas have higher water retention capabilities.

The statistical analysis showed that plant properties are significantly correlated with crop yield. Such correlations, however, are low for those data acquired in the early vegetative stage. This is due to the non-uniform plant distribution at emergence⁶⁰ and to the presence of areas with low initial plant spatial abundance but have improved during the growing season. Such improvement depends on soil condition, temperature, as well as being in competition among plants⁶⁰. On the other hand, the early assessment showed several areas identified as potentially anomalous that persisted during the growing season, with correlations increased during the growing seasons, proving the efficacy in performing early assessment. Additionally, early assessment conducted with UAV-based imaging together with photogrammetry techniques, allowed us to derive the topographical gradient, which represented an important driver for water management with strong implications on both plant development and soil–plant relationships. In the late season, we can see a decrease of the correlation and statistical significance between yield and plant height in September (see plant height in September 19th), in particular in the east and center areas. The decrease in correlation is due to the presence of areas in which the soybeans are approaching

	Date	West		Center		East	
		r	Corr	r	Corr	r	Corr
Yield versus Plant spatial abundance	2018-05-28	0.15***	0.14 (-)	0.02 (-)	0.06 (-)	0.15***	0.07 (-)
	2018-06-25	0.53***	0.56**	0.26***	0.28*	0.23***	0.22*
	2018-07-23	0.67***	0.69**	0.38***	0.40**	0.32***	0.30*
Yield versus Plant vigor	2018-05-28	0.17*	0.16 (-)	0.04 (-)	0.07 (-)	0.17*	0.09 (-)
	2018-06-25	0.54***	0.57**	0.26***	0.27**	0.23***	0.22*
	2018-07-23	0.67***	0.69**	0.37***	0.39**	0.32***	0.29*
Yield versus Plant height	2018-06-25	0.09*	0.21**	0.22***	0.20 (-)	0.19***	0.21**
	2018-07-23	0.60***	0.57**	0.42*	0.46**	0.46***	0.40**
	2018-09-19	0.53***	0.41**	0.32*	0.37**	0.14*	0.17 (-)
Yield versus Soil EC		0.12*	0.06**	-0.24***	-0.21 (-)	-0.11**	-0.11**
Yield versus elevation		-0.14*	-0.03 (-)	0.02 (-)	0.01 (-)	0.16*	0.14 (-)

Table 3. Pearson's (r) and corrected Pearson's (corr) coefficients computed between the yield, plant properties, soil EC_a, and elevation. The table reports the correlations computed for the east, center, and west areas. Statistical significance is given by * $p < .05$, ** $p < .01$, *** $p < .001$, (-) for non significance.

the maturity stage, when leaves turn yellow to then fall. Also, plants that have grown high tend to fold, causing a general decrease in the UAV-estimated plant height. The UAV acquisition during the September period could potentially be used to retrieve information on the spatial variability of maturity rate, and potentially be used to optimize planting in the next season.

The methodological framework developed in this study—based on time-series analysis of UAV-based images and geophysical data—was able to capture the dynamic plant-soil spatial patterns, and can be easily implemented for precision agriculture as a tool for early assessment and crop monitoring. From our analysis, multitemporal acquisitions are necessary to understand the heterogeneity in soil-plant signatures associated with a crop field. Remote sensing acquisitions should be planned accordingly to the crop growth-schedule to acquire data during critical stages. However, we recognize the difficulty in acquiring a such high-resolution dense data stream. As such, the combination of UAV and satellite imagery could be a good alternative. While the UAV's high resolution is necessary to perform an early assessment of sprout coverage, providing insight on possible anomalous areas that could be treated timely, multiple satellite acquisitions can provide insight on the possible plant degradation. Particular attention should be given to acquisitions during the late maturity stage, since vegetation indices could provide misleading information due to plants phenology changes during that period. Additionally, an early geophysical survey can guide the ground sampling in order to assess soil physical-chemical properties to optimize amendment applications. Such assessment could be performed once a year prior to planting since soil texture would not change over time, while a sensor network could be used to track soil moisture variability during the growing season.

While this study focused on a soybean crop, the methodology is general and it can be applied to different crops to provide a better understanding of the underlying causes of a possible spatial variability in plant growth, and provide insights for the next season.

Conclusion

This study explored the joint use of remote sensing and geophysical data to investigate soil-plant interactions in a soybean crop field. We proposed a novel pipeline to extract informative products, such as plant spatial abundance and plant-specific vigor from multitemporal high-resolution UAV data to capture plant dynamics since the early-stage of the growing season. We exploited an EMI system to measure high-resolution and spatially extended soil properties by measuring soil EC_a.

The spatial analysis of the multisource data stream showed a strong spatial heterogeneity in soil properties. A similar spatial pattern was captured by plant spatial abundance and plant vigor products already at the early-stage, indicating the strong impact of soil properties on plant development.

In particular, a significant negative correlation between plant properties and soil EC_a indicated that increased amount of clay had negative impact on plant development. In addition, our analysis showed that the spatiotemporal variations in soil moisture, imaged by temporal changes in EC_a and influenced by topography, impacted the plant development. Thus, the topographic gradient represented a major control on the water management, with implications on the plant development and crop yield.

The results of this study showed that an effective integration of remote sensing, surface electromagnetic geophysics, and point measurements enables a better understanding of the dynamics that characterize soil-plant interactions in agriculture ecosystems. Furthermore, the ability of the developed methodology in characterizing above and below surface properties would provide valuable information to guide crop management from the early season and throughout the entire growing season.

Received: 22 May 2020; Accepted: 8 March 2021

Published online: 29 March 2021

References

- Gebbers, R. & Adamchuk, V. I. Precision agriculture and food security. *Science* **327**, 828–831 (2010).
- Brisco, B., Brown, R. J., Hirose, T., McNairn, H. & Staenz, K. Precision agriculture and the role of remote sensing: a review. *Can. J. Remote Sens.* **24**, 315–327 (1998).
- Mulla, D. J. Twenty five years of remote sensing in precision agriculture: Key advances and remaining knowledge gaps. *Biosyst. Eng.* **114**, 358–371 (2013).
- Bastiaanssen, W. G. M., Molden, D. J. & Makin, I. W. Remote sensing for irrigated agriculture: examples from research and possible applications. *Agric. Water Manag.* **46**, 137–155 (2000).
- Seelan, S. K., Laguetta, S., Casady, G. M. & Seielstad, G. A. Remote sensing applications for precision agriculture: a learning community approach. *Remote Sens. Environ.* **88**, 157–169 (2003).
- Bagheri, N., Ahmadi, H., Alavipanah, S. K. & Omid, M. Multispectral remote sensing for site-specific nitrogen fertilizer management. *Pesqui. Agropecuária Bras.* **48**, 1394–1401 (2013).
- Zhang, C. & Kovacs, J. M. The application of small unmanned aerial systems for precision agriculture: a review. *Precis. Agric.* **13**, 693–712 (2012).
- Gago, J. *et al.* UAVs challenge to assess water stress for sustainable agriculture. *Agric. Water Manag.* **153**, 9–19 (2015).
- Colomina, I. & Molina, P. Unmanned aerial systems for photogrammetry and remote sensing: a review. *ISPRS J. Photogramm. Remote Sens.* **92**, 79–97 (2014).
- Berni, J., Zarco-Tejada, P. J., Suarez, L. & Fereres, E. Thermal and narrowband multispectral remote sensing for vegetation monitoring from an unmanned aerial vehicle. *IEEE Trans. Geosci. Remote Sens.* **47**, 722–738 (2009).
- Das, J. *et al.* Devices, systems, and methods for automated monitoring enabling precision agriculture. in *2015 IEEE International Conference on Automation Science and Engineering (CASE)* 462–469 (IEEE, 2015). <https://doi.org/10.1109/CoASE.2015.7294123>.
- Khanal, S., Fulton, J. & Shearer, S. An overview of current and potential applications of thermal remote sensing in precision agriculture. *Comput. Electron. Agric.* **139**, 22–32 (2017).
- Swain, K. C., Thomson, S. J. & Jayasuriya, H. P. W. Adoption of an unmanned helicopter for low-altitude remote sensing to estimate yield and total biomass of a rice crop. *Trans. ASABE* **53**, 21–27 (2010).
- Holman, F. *et al.* High throughput field phenotyping of wheat plant height and growth rate in field plot trials using UAV based remote sensing. *Remote Sens.* **8**, 1031 (2016).
- Shakoor, N., Lee, S. & Mockler, T. C. High throughput phenotyping to accelerate crop breeding and monitoring of diseases in the field. *Curr. Opin. Plant Biol.* **38**, 184–192 (2017).
- Gnädinger, F. & Schmidhalter, U. Digital counts of maize plants by Unmanned Aerial Vehicles (UAVs). *Remote Sens.* **9**, 96 (2017).
- Koh, J. C. O., Hayden, M., Daetwyler, H. & Kant, S. Estimation of crop plant density at early mixed growth stages using UAV imagery. *Plant Methods* **15**, 83 (2019).
- Jin, X., Liu, S., Baret, F., Hemerlé, M. & Comar, A. Estimates of plant density of wheat crops at emergence from very low altitude UAV imagery. *Remote Sens. Environ.* **198**, 105–114 (2017).
- Varela, S. *et al.* Early-season stand count determination in corn via integration of imagery from unmanned aerial systems (UAS) and supervised learning techniques. *Remote Sens.* **10**, 343 (2018).
- Barry J. Allred, Jeffrey J. Daniels, & M. Reza Eshani. *Handbook of Agricultural Geophysics*. (CRC Press, 2008).
- Dafflon, B., Hubbard, S. S., Ulrich, C. & Peterson, J. E. Electrical conductivity imaging of active layer and permafrost in an arctic ecosystem, through advanced inversion of electromagnetic induction data. *Vadose Zone J.* **12**, 1598 (2013).
- Hubbard, S. S. *et al.* Quantifying and relating land-surface and subsurface variability in permafrost environments using LiDAR and surface geophysical datasets. *Hydrogeol. J.* **21**, 149–169 (2013).
- Hubbard, S. S. & Linde, N. Hydrogeophysics. in *Treatise on Water Science* 401–434 (Elsevier, 2011). <https://doi.org/10.1016/B978-0-444-53199-5.00043-9>.
- Yao, R. *et al.* Digital mapping of soil salinity and crop yield across a coastal agricultural landscape using repeated electromagnetic induction (EMI) surveys. *PLoS ONE* **11**, 1–20 (2016).
- Korsaeth, A. Soil apparent electrical conductivity (ECa) as a means of monitoring changes in soil inorganic N on heterogeneous morainic soils in SE Norway during two growing seasons. *Nutr. Cycl. Agroecosystems* **72**, 213–227 (2005).
- Koszinski, S., Miller, B. A., Hierold, W., Haelbich, H. & Sommer, M. Spatial modeling of organic carbon in degraded peatland soils of Northeast Germany. *Soil Sci. Soc. Am. J.* **79**, 1496 (2015).
- Moral, F. J., Terrón, J. M. & Silva, J. R. M. Delineation of management zones using mobile measurements of soil apparent electrical conductivity and multivariate geostatistical techniques. *Soil Tillage Res.* **106**, 335–343 (2010).
- Stadler, A. *et al.* Quantifying the effects of soil variability on crop growth using apparent soil electrical conductivity measurements. *Eur. J. Agron.* **64**, 8–20 (2015).
- Wainwright, H. M. *et al.* Identifying multiscale zonation and assessing the relative importance of polygon geomorphology on carbon fluxes in an Arctic tundra ecosystem. *J. Geophys. Res. Biogeosciences* **120**, 788–808 (2015).
- Falco, N. *et al.* Investigating microtopographic and soil controls on a mountainous meadow plant community using high-resolution remote sensing and surface geophysical data. *J. Geophys. Res. Biogeosciences* <https://doi.org/10.1029/2018JG004394> (2019).
- Dafflon, B. *et al.* Coincident above- and below-ground autonomous monitoring to quantify co-variability in permafrost, soil and vegetation properties in Arctic Tundra. *J. Geophys. Res. Biogeosciences* **3**, 1–22. <https://doi.org/10.1002/2016JG003724> (2017).
- Rudolph, S. *et al.* Linking satellite derived LAI patterns with subsoil heterogeneity using large-scale ground-based electromagnetic induction measurements. *Geoderma* **241–242**, 262–271 (2015).
- von Hebel, C. *et al.* Understanding soil and plant interaction by combining ground-based quantitative electromagnetic induction and airborne hyperspectral data. *Geophys. Res. Lett.* **45**, 7571–7579 (2018).
- Hubbard, S. S. *et al.* Estimation of soil classes and their relationship to grapevine vigor in a Bordeaux vineyard: advancing the practical joint use of electromagnetic induction (EMI) and NDVI datasets for precision viticulture. *Precis. Agric.* <https://doi.org/10.1007/s11119-021-09788-w> (2021).
- Liu, S. *et al.* A method to estimate plant density and plant spacing heterogeneity: application to wheat crops. *Plant Methods* **13**, 38 (2017).
- QGIS Development Team. *QGIS Geographic Information System*. (QGIS Association, 2020).
- Runkle, B. R. K. *et al.* Delta-flux: an Eddy covariance network for a climate-smart lower Mississippi basin. *acl* **2**, 15 (2017).
- Soil Survey Staff, Natural Resources Conservation Service & United States Department of Agriculture. *Web Soil Survey*. <http://websoilsurvey.sc.egov.usda.gov/>. (2017).
- Boru, G. Responses of Soybean to oxygen deficiency and elevated root-zone carbon dioxide concentration. *Ann. Bot.* **91**, 447–453 (2003).
- Walker, W. R. *Guidelines for designing and evaluating surface irrigation systems*. vol. 45 (Food and Agriculture Organization of the United Nations, 1989).
- Syednasrollah, B. *et al.* Tracking vegetation phenology across diverse biomes using Version 2.0 of the PhenoCam Dataset. *Sci. Data* **6**, 222 (2019).
- Escobar Villanueva, J. R., Iglesias Martínez, L. & Pérez Montiel, J. I. DEM generation from fixed-wing UAV imaging and LiDAR-derived ground control points for flood estimations. *Sensors* **19**, 3205 (2019).

43. Falco, N., Xia, J., Kang, X., Li, S. & Benediktsson, J. A. Supervised classification methods in hyperspectral imaging—recent advances. in *Hyperspectral Imaging* vol. 32 247–279 (Elsevier, 2020).
44. Falco, N., Benediktsson, J. A. & Bruzzone, L. Spectral and spatial classification of hyperspectral images based on ICA and reduced morphological attribute profiles. *IEEE Trans. Geosci. Remote Sens.* **53**, 6223–6240 (2015).
45. Cavallaro, G., Falco, N., Dalla Mura, M. & Benediktsson, J. A. Automatic attribute profiles. *IEEE Trans. Image Process.* **26**, 1859–1872 (2017).
46. Benediktsson, J. A. *et al.* Remote Sensing Data Fusion: Markov Models and Mathematical Morphology for Multisensor, Multiresolution, and Multiscale Image Classification. in *Mathematical Models for Remote Sensing Image Processing* 277–323 (Springer International Publishing, 2018). https://doi.org/10.1007/978-3-319-66330-2_7.
47. Chang, C.-C. & Lin, C.-J. LIBSVM: a library for support vector machines. *ACM Trans. Intell. Syst. Technol.* **2**, 1–27 (2011).
48. Anderson, H. *et al.* Using ordinary digital cameras in place of near-infrared sensors to derive vegetation indices for phenology studies of high arctic vegetation. *Remote Sens.* **8**, 847 (2016).
49. Corwin, D. L. & Lesch, S. M. Apparent soil electrical conductivity measurements in agriculture. *Comput. Electron. Agric.* **46**, 11–43 (2005).
50. Sheets, K. R. & Hendrickx, J. M. H. Noninvasive soil water content measurement using electromagnetic induction. *Water Resour. Res.* **31**, 2401–2409 (1995).
51. Ma, R., McBratney, A., Whelan, B., Minasny, B. & Short, M. Comparing temperature correction models for soil electrical conductivity measurement. *Precis. Agric.* **12**, 55–66 (2011).
52. Hayley, K., Bentley, L. R., Gharibi, M. & Nightingale, M. Low temperature dependence of electrical resistivity: Implications for near surface geophysical monitoring. *Geophys. Res. Lett.* **34**, 61 (2007).
53. Clifford, P., Richardson, S. & Hemon, D. Assessing the significance of the correlation between two spatial processes. *Biometrics* **45**, 123 (1989).
54. Moran, P. A. P. Notes on continuous stochastic phenomena. *Biometrika* **37**, 17–23 (1950).
55. Osorio, F., Vallejos, R. & Cuevas, F. SpatialPack: Computing the Association Between Two Spatial Processes. *ArXiv161105289 Stat* (2016).
56. MATLAB. *version 9.2.0.556344 (R2017a)*. (The MathWorks Inc., 2010).
57. Hinckley, E.-L.S., Barnes, R. T., Anderson, S. P., Williams, M. W. & Bernasconi, S. M. Nitrogen retention and transport differ by hillslope aspect at the rain-snow transition of the Colorado Front Range. *J. Geophys. Res. Biogeosciences* **119**, 1281–1296 (2014).
58. Hinckley, E.-L.S. *et al.* Aspect control of water movement on hillslopes near the rain-snow transition of the Colorado Front Range. *Hydrol. Process.* **28**, 74–85 (2014).
59. Devadoss, J. *et al.* Remote sensing-informed zonation for understanding snow, plant and soil moisture dynamics within a Mountain Ecosystem. *Remote Sens.* **12**, 2733 (2020).
60. Olsen, J., Kristensen, L. & Weiner, J. Influence of sowing density and spatial pattern of spring wheat (*Triticum aestivum*) on the suppression of different weed species. *Weed Biol. Manag.* **6**, 165–173 (2006).

Acknowledgments

The authors acknowledge support for this research work the Laboratory Directed Research and Development (LDRD) funding from Lawrence Berkeley National Laboratory, provided by the Director, Office of Science, of the U.S. Department of Energy under Contract No. DE-AC02-05CH11231. Authors want to thank Glennoe Farms LLC for providing crop yield data, the Fayetteville Agriculture Diagnostic Laboratory of the University of Arkansas for the soil analysis, and ARVA Intelligence for supporting the publication costs.

Author contributions

N.F., H.M.W., B.D., C.U., J.B.B., J.A.M., S.S.H. conceived the study and planned the data collection; N.F., H.M.W., B.D., C.U., F.S., M.W., J.D.C., R.G.H. designed and carried out the data collection; N.F., J.P., H.M.W., B.D., C.U. processed, handled, and analysed the data; N.F. led the writing of the manuscript and prepared the figures. All authors reviewed the manuscript and gave final approval for publication.

Competing interests

The authors declare no competing interests.

Additional information

Supplementary Information The online version contains supplementary material available at <https://doi.org/10.1038/s41598-021-86480-z>.

Correspondence and requests for materials should be addressed to N.F.

Reprints and permissions information is available at www.nature.com/reprints.

Publisher's note Springer Nature remains neutral with regard to jurisdictional claims in published maps and institutional affiliations.



Open Access This article is licensed under a Creative Commons Attribution 4.0 International License, which permits use, sharing, adaptation, distribution and reproduction in any medium or format, as long as you give appropriate credit to the original author(s) and the source, provide a link to the Creative Commons licence, and indicate if changes were made. The images or other third party material in this article are included in the article's Creative Commons licence, unless indicated otherwise in a credit line to the material. If material is not included in the article's Creative Commons licence and your intended use is not permitted by statutory regulation or exceeds the permitted use, you will need to obtain permission directly from the copyright holder. To view a copy of this licence, visit <http://creativecommons.org/licenses/by/4.0/>.

© The Author(s) 2021